A Two-Dimensional Zirconium Carbide by Selective Etching of Al3C3 from Nanolaminated Zr3Al3C5

Jie Zhou, Xianhu Zha, Fan Y. Chen, Qun Ye, Per Eklund, Shiyu Du and Qing Huang

Linköping University Post Print

N.B.: When citing this work, cite the original article.

A New Two-Dimensional Zirconium Carbide MXene by Selective Etching of Al₃C₃ from Nanolaminated Zr₃Al₃C₅

Jie Zhou, [+] *Xianhu Zha,* [+] *Fan Y. Chen, Qun Ye, Per Eklund, Shiyu Du,* * *and Qing Huang* *

Abstract: We report the room temperature synthesis of a new two-dimensional (2D) zirconium-containing carbide, $Zr_3C_2T_z$ MXene. In contrast to traditional preparation of MXene, the layered ternary $Zr_3Al_3C_5$ material instead of MAX phases is used as source under hydrofluoric acid treatment. The structural, mechanical and electronic properties of the synthesized 2D carbide are investigated combined with first-principles density functional calculations. A comparative study on the structrual stability of our obtained 2D $Zr_3C_2T_z$ and $Ti_3C_2T_z$ MXenes at elevated temperatures is performed. The obtained 2D $Zr_3C_2T_z$ exhibits relatively better ability to maintain 2D nature and strucural integrity compared to Ti-based Mxene. The difference in structural stability under high temperature condition is explained by theoretical investigation on binding energy.

During the past decade, two-dimensional (2D) materials have attracted extensive attention due to their high surface area to volume ratio, unique electronic structures and physiochemical properties derived from their low dimensionality.[1-7] Graphene, the most studied 2D material with ultrahigh mechanical strength,[8-9] excellent electronic and thermal conductivities,[1, 10-11] exhibits potential applications in electrochemical energy storage, transparent electrodes, and nano-composites.[12] However, due to its intrinsic zero bandgap and simple chemistry, applications of graphene are restricted in some aspects, such as field effect transistors.[10] Thus, investigations on other 2D materials are performed, especially for those 2D materials with two or more composition elements, such as metal oxide, layered metal chalcogenides (LMDCs), hexagonal boron nitride(BN), hydroxides, *etc*.[6, 13] In recent years, a new class of 2D materials called MXenes, have emerged[14] Members in this family are described by the general formula of $M_{n+1}X_nT_z$ (wherein M is an early transition metal, X is C and/or N, n is 1, 2, 3, and T_z denotes surface terminated functional groups).[14] Generally, MXenes are produced by the selective etching of Al layers from their parental layered ternary MAX phases, a large group which comprises more than 70 members.[15-16] Through selective etching of aluminium layers, experimental investigations have successfully identified about 10 different MXenes, $Ti_3C_2T_z$, Ti_2CT_z,

$Ta_4C_3T_z$, $TiNbCT_z$, $(V_{0.5},Cr_{0.5})_3C_2T_z$, Ti_3CNT_z, Nb_2CT_z, V_2CT_z, and $Nb_4C_3T_z$.[14, 17] Most of the synthesized MXenes are metallic,[18] hydrophilic, and predicted to have high elastic moduli, implying potential application as reinforcement of polymer.[19-20] The existance of Dirac electrons in some MXenes has also been theoretically predicted .[21] Moreover, similar to graphene, MXenes are promising candidate electrode materials for lithium-ion batteries and supercapacitors by facile intercalation of Li ions into the MXene layers.[22-27] Recently, considerable efforts have been made to further expand the family of 2D carbides. On the basis of a substitutional solid solution method, Gogotsi and Barsoum *et al*.[28] successfully synthesized $Mo_2TiC_2T_z$, $Mo_2Ti_2C_3T_z$, and $Cr_2TiC_2T_z$ MXenes, and surface dependent electrochemical behaviors in the case of $Mo_2TiC_2T_z$ have been revealed. Moreover, Mo_2CT_z MXene [29] has been synthesized through selective etching of gallium (Ga) from a thin film of the new ternary nanolaminated Mo_2Ga_2C.[30-31] Besides, large-area high-quality 2D α-Mo_2C, WC, and TaC crystals have been fabricated by a chemical vapour deposition (CVD) process.[32] However, potential MXene compounds in materials systems where Al-containing MAX phases are not established, such as Hf_2C and Zr_2C, are yet to be produced.

Herein, for the first time, we report the preparation of Zr-containing 2D carbide based on selective extraction of Al-C units from an alternative layered ternary $Zr_3Al_3C_5$, benefiting from the relatively weakly bonded and hydrolysis-prone Al-C layers in the $Zr_3Al_3C_5$ crystal structure. $Zr_3Al_3C_5$ is a typical member of the layered ternary and quaternary transition-metal carbides beyond MAX phases; holding a common formula of $M_nAl_3C_2$ and $M_n[Al(Si)]_4C_3$ (where M= Zr or Hf, n = 1-3).[33] The crystal structure of these carbides can be described as an intergrowth structure of layers with hexagonal MC and Al_4C_3-like $Al_3C_2/[Al(Si)]_4C_3$ sharing a carbon monolayer at their coupling boundaries.[33]

We prepared $Zr_3Al_3C_5$ by an in situ reactive pulsed electric current sintering (PECS) process (see the Supporting Information, SI, Section 1, S1) similar to our previous study.[34] The exfoliation process of $Zr_3Al_3C_5$ was implemented by using concentrated hydrofloric (HF) acid. The structural, electronic and elastic properties of the as-exfoliated nanosheets were investigated combined with first-principles density functional calculations. Moreover, the structural stability of the as-prepared nanosheets at elevated temperatures were studied and compared with that of $Ti_3C_2T_z$ MXenes.

[*] J. Zhou, [+] X. H. Zha, [+] ,Fan Y. Chen, Q. Ye, Prof. S. Y. Du, Prof. Q. Huang
  Engineering Laboratory of Specialty Fibers and Nuclear Energy Materials (FiNE), Ningbo Institute of Materials Engineering and Technology, Chinese Academy of Sciences, Ningbo,Zhejiang 315201, China
  E-mail: huangqing@nimte.ac.cn, dushiyu@nimte.ac.cn
  Prof. P. Eklund
  Thin Film Physics Division, Linköping University, IFM, 581 83 Linköping, Sweden
[+] These authors contributed equally to this work.

  Supporting information for this article is given via a link at the end of the document.
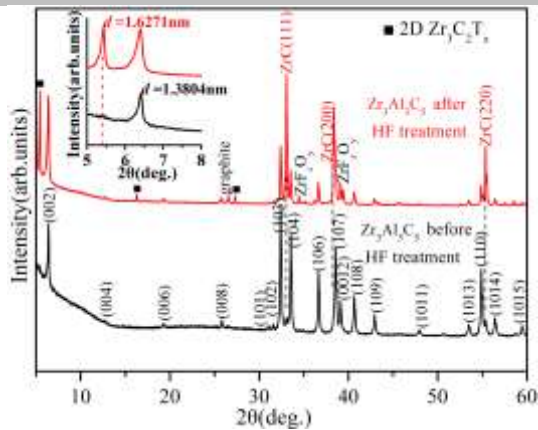
Figure 1 X-ray diffraction patterns of $Zr_3Al_3C_5$ before and after HF treatment.

As shown in Figure 1, the as-fabricated powders are predominantly single phase $Zr_3Al_3C_5$ besides a minor amount of ZrC impurities. When the $Zr_3Al_3C_5$ powders (300 mesh) were immersed in 50 wt.% hydrofluric acid (HF) aqueous solution, bubbles, possibly to be H_2 and CH_4, were observed, which had also been observed during the formation of Ti_3C_2 MXenes.[19] Details of the etching process can be found in SI, S1. The corresponding XRD result of the etched powders is plotted in Figure 1. The peak intensities originating from the parent $Zr_3Al_3C_5$ crystal decrease substantially after immersion in the concentrated HF solution. More importantly, the (0002) peak downshifts to a lower angle of $2\theta = 5.43°$, attributing to an enlarged c lattice parameter of 32.53 Å , from the original 27.73 Å of $Zr_3Al_3C_5$ crystal. The newly emerged low angle (0002) peak is typical for most reported HF-etched MXenes[17, 19], another two (000l) peaks located at $2\theta = 16.32°$, and $2\theta = 27.24°$ can also be detected, respectively. Unlike the broad peaks typical of HF-etched MXenes, three newly formed lower angle (000l) peaks in our present study shows relatively sharper shape and increased intensity, which is more typical of intercalated MXenes.[27, 35] It is thus reasonable to speculate that the enlarged c lattice parameter of 32.53 Å might be associated with spontaneous intercalation during the etching process.**[27]** Moreover, the small amount of rock-salt-like cubic ZrC impurities presented in the raw $Zr_3Al_3C_5$ powders did not react with HF and the relative intensity of their peaks increases apparently after HF-treatment, probably due to a drastic loss of parent $Zr_3Al_3C_5$ and possibly formation of less ordered phase.

The SEM images of $Zr_3Al_3C_5$ after the HF treatment (Figure 2a-b) confirm exfoliation of individual grain along the basal planes. Grain with accordion morphology are observed, which is similar to what was reported for Ti_3AlC_2.[19] The corresponding energy dispersive spectrum (EDS) results obtained from an area of about 2000 μm^2 show the presence of Zr, C, O, F, and corresponding substantial decrease of the Al signal (Figure S4), indicates the removal of Al-C layer from the original crystal structure.[19]
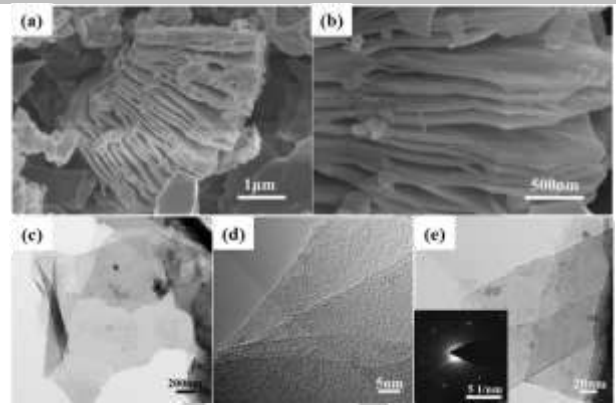

Figure 2 (a)-(b)SEM images of the powders after HF treatment, showing the exfoliated grain and accordion-like structure; (c)Typical bright-field TEM images of the 2D $Zr_3C_2T_z$ after ultrasonication; (d)TEM image of few-layered $Zr_3C_2T_z$ and (e) TEM image of a scrolled $Zr_3C_2T_z$ nanosheet. Left inset in (e) is a SAED pattern showing the reserved hexagonal basal plane symmetry.

Additionaly, the obtained Zr:Al molar ratio was larger than 3.0:0.9. In consideration of the possible residual aluminium fluoride,[26] it is reasonable to assume that more than 70 at% of the $Zr_3Al_3C_5$ has been transformed.[26] TEM micrographs of HF-etched $Zr_3Al_3C_5$ after sonication are shown in Figure 2c-e, depicting electron-transparent thin morphology and a few layer structures, EDS results of the same flake confirm the presence of Zr, C, and O with no aluminium (Figure S5). Moreover, the thin nanosheet is presented to be flexible and folding, which is similar to those of graphene and 2D MXenes.[19, 36] The corresponding selected area electron diffraction (SAED, inset in Figure 2e) shows the hexagonal symmetry of the as-obtained nanosheets.[33]
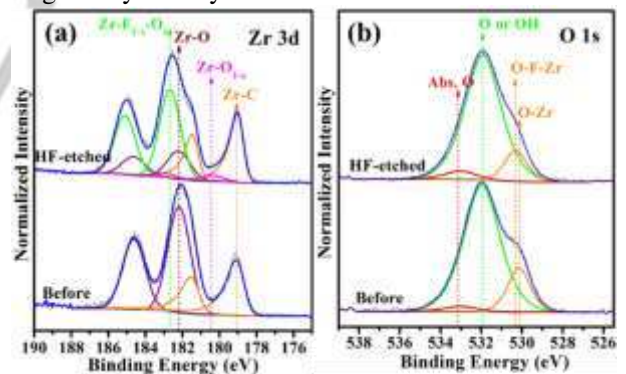

Figure 3 High-resolution XPS spectra of samples before and after etching treatment in the (a) Zr 3d region and (b) O 1s region.

The Zr 3d and O 1s X-ray photoelectron spectroscopy (XPS) results before and after HF treatment are shown in Figure 3a. The presence of Zr-C and Zr-O bonds before treatment matches previous works on ZrC[37] (Figure 3a-b). After HF treatment, the fitted results of XPS spectrum in the Zr 3d region consistently show the appearence of mixed Zr-F-O[38], partially oxidized Zr-O[37], and Zr-C bonds[37] (Figure 3a). In addition, the corresponding fitted results in the O 1s region further comfirm the presence of mixed Zr-F-O[38] in etched samples, partially oxidized Zr-O bonds and OH groups[37] (Figure 3b) are also presented in both spectra, indicating the potential formation of Zr_3C_2 and a mixture of F and

OH surface groups[26]. Moreover, Zr-C bond emerges in the C 1s region accordingly.[38](Figure S1).

Based on the aformentioned results, it is reasonable to deduce that the relatively weakly bonded and easily hydrolysed Al-C slabs in $Zr_3Al_3C_5$ were selectively etched when immersed in 50% HF solution, and the surface of left Zr-based layer was functionalized by OH and F surface groups.
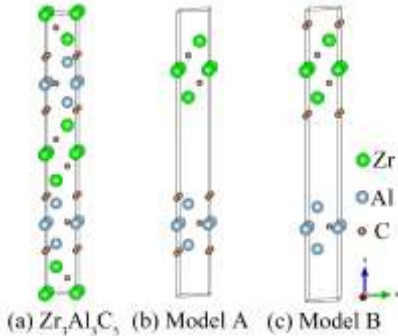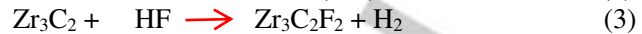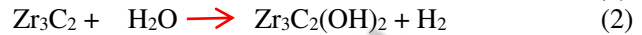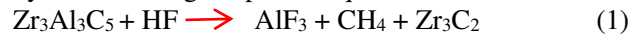
Figure 4 (a) the unit cell of $Zr_3Al_3C_5$; (b) Model A: $Zr_3C_2+Al_3C_3$; (c) Model B: $Zr_3C_4+Al_3C$.

It should be noted that, there is one 2D carbon atomic plane shared by Zr-C layers and Al_3C_2 slab in the unit cell of $Zr_3Al_3C_5$ as mentioned above. To exactly verify the affiliation of the C atoms during the etching process and thus determine the final reaction product, density functional theory (DFT)-based geometry optimization was carried out. Figure 4a shows the crystal structure of parent $Zr_3Al_3C_5$.[33] Two models named Model A and Model B are considered and given in Figure 4b and Figure 4c, respectively. In Model A, the concerned carbon layers combined with aluminum atoms, which means the dissolved layers are Al_3C_3 in hydrofluoric acid and our product is $Zr_3C_2T_z$ MXene. Reversely, Model B shows the other possibility that the carbon layers are retained after hydrofluoric acid treatment. In these two models, a vacuum layer of 10 Å between the separated monolayers is used to eliminate the layer interaction. After optimization, the total energy of Model A is determined to be -80.03 eV, and that of model B is -76.85 eV. Evidently, Model A is more stable than Model B, which implies that our monolayer product is 2D $Zr_3C_2T_z$. On the basis of the above analysis, the structural transformation process of $Zr_3Al_3C_5$ under HF treatment is illustrated in Figure S2. since the thickness of the dissolved Al_3C_3 slab is much thicker than that of monolayer aluminum in the unit cell of MAX phase[19], more interlayer space are provided. Furthermore, the relatively small lateral size of the obtained sheets also favors the occurance of intercalation process. It should be noted that the large observed c lattice parameters (32.53Å) in our present study can be attributed to spontaneous intercalation of water molecules[17, 26, 39] and cointercalation of reaction products into the 2D $Zr_3C_2T_z$ during the etching process, which have been reported for the preparation of V_2C，Nb_2C, and Mo_2C MXenes.[26, 29]

On the basis of the above experimental and calculated results, the chemical reactions occurred during the etching process of $Zr_3Al_3C_5$ can be reasonably described by the following simplified equations:

$$Zr_3Al_3C_5 + HF \longrightarrow AlF_3 + CH_4 + Zr_3C_2 \qquad (1)$$
$$Zr_3C_2 + H_2O \longrightarrow Zr_3C_2(OH)_2 + H_2 \qquad (2)$$
$$Zr_3C_2 + HF \longrightarrow Zr_3C_2F_2 + H_2 \qquad (3)$$

which is similar to the reactions occurred during the HF etching process of Ti_3AlC_2 powders.[19]

To further explore the exact thickness of the as-etched $Zr_3C_2T_z$, AFM measurement was carried out for the $Zr_3C_2T_z$ samples after sonication (Figure S3). The thickness of the Zr3C2Tz was approximately 3.5 nm (nearly corresponds to two layers of $Zr_3C_2T_z$), basically approximate the calculated c value based on XRD patterns (Figure 1), and the lateral size of the nanosheets was approximately 1.5−2μm.
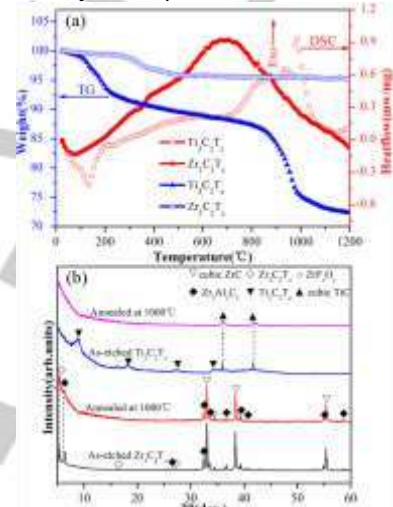
Figure 5 (a) TG and DSC curves of Ti_3C_2 and 2D $Zr_3C_2T_z$ from RT to 1200°C in argon atmosphere, (b) X-ray diffraction patterns of Ti_3C_2 MXene and 2D $Zr_3C_2T_z$ before and after annealed in vacuum at 1000°C for 2h.

The structural stability of 2D materials is important for their practical applications at elevated temperatures. Thus a comparative study on the structural stability of 2D $Ti_3C_2T_z$ and $Zr_3C_2T_z$ MXenes under high temperatures was performed. Figure 5a shows thermal gravity (TG) and differential scanning calorimetry (DSC) curves of $Ti_3C_2T_z$ and $Zr_3C_2T_z$ from room temperatue to 1200°C in argon atmosphere. In the case of $Ti_3C_2T_z$, the first stage of mass loss about 7% can be observed in the 50-200°C temperature range. Concomitantly, an endothermic peak emerges at 133°C in the corresponding DSC curve. Regarding 2D $Zr_3C_2T_z$ MXene, one stage of mass loss of about 4% in the 50-500°C temperature range emerges in TG curve. In addition, an endothermic peak appears at 71°C in its corresponding DSC curve. It is reasonable to conclude that the first stage in both cases is due to the removal of physically absorbed water[26, 40-41] and intercalated crystal water.[35] Above 500°C, a broad exothermic peak at about 700°C can be identified in DSC curve of 2D $Zr_3C_2T_z$, and without apprent mass loss in TG curve from 500°C to 1200°C. This slow exothermic process might be related to the growth of nanocrystals. In the case of $Ti_3C_2T_z$, an apparent mass loss of about 6% occurred in the 200-800°C temperature range, indicating

the potential dehydroxylation of residual-isolated OH groups bonded with the metal-terminated surface.[41] It is followed by an abrupt mass loss of about 14% from 800 to 1000°C. Simultaneously, a relatively sharp exothermic peak appears at about 984°C in DSC curves, likely related to crystal structure transformation.[15, 40] Note that in the case of $Zr_3C_2T_z$, the relatively less significant mass loss in TG curves could be related to the influence of the more stable pre-existing cubic ZrC and residual $Zr_3Al_3C_5$ second phases presented in the HF-treated powder mixture.

To further gain insight in the above distinct thermal behaviors between the $Ti_3C_2T_z$ and $Zr_3C_2T_z$ MXenes in the 500-1000°C temperature range, XRD analysis was performed. As shown in Figure 5b, it can be seen that characteristic diffraction peaks belong to hexagonally symmetrical Ti_3C_2 MXenes disappeared and only cubic TiC can be detected after two hours vacuum annealing at 1000°C. This indicates apparent decrease of order of Ti_3C_2 MXenes along c axis or that a structural transformation occurred. In the case of $Zr_3C_2T_z$ (Figure 5b), peaks corresponding to $Zr_3C_2T_z$ still can be detected, but with decreases intensity and broadened, indicating removal of intercalated species, surface groups, and less order along c-axis. Moreover, diffraction peaks related to residual $Zr_3Al_3C_5$ are also decreased to some extent, which could be related to initial structural damage occurred during the HF etching process and subsequent high temperature pertubation.
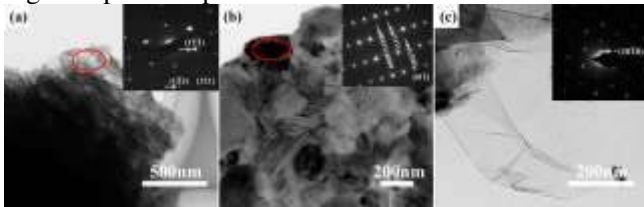

Figure 6 (a)-(b)Typical bright-field TEM images of the vacuum annealed $Ti_3C_2T_z$ after ultrasonication, insets in (a)-(b) are SAED patterns corresponding to areas marked in red; (c) Typical bright-field TEM image of the vacuum annealed $Zr_3C_2T_z$ after ultrasonication, inset in (c) is SAED pattern of the observed flake.

To exactly identify the above structural evolution, we performed TEM observation of the samples after vacuum annealing treatment. A TEM image of ultrasonicated $Ti_3C_2T_z$ nanosheets (Figure 6a) shows that their 2D nature and structural integrity to be partially disturbed. The corresponding SAED (Inset in Figure 6a) can be indexed as cubic TiC_x, indicating that a structural transformation has occured. In fact, similar hexagonal-cubic structural transformation was observed in previous studies, in those cases, bulk Ti_3SiC_2 was immersed in molten aluminium[42] or cryolite[43] at high temperatures. Figure 6b shows that some nanocrystals formed on the initial $Ti_3C_2T_z$ flakes, SAED analysis (Inset in Figure 6b) reveals the formation of rutile TiO_2, which might be related to the oxidation of nanosheet from oxidizing surface groups or residual oxygen in vacuum. As shown in Figure 6c, nanosheets of $Zr_3C_2T_z$ after HT treatment remain their quite thin and uniform morphology, which is similar to that of the untreated state. The corresponding

SAED (Inset in Figure 6c) confirms the original hexagonal symmetry. It is thus reasonable that $Zr_3C_2T_z$ exhibits better structural integrity, and remains 2D, in our present temperature range, which agree with the above TG-DSC and XRD results (Figure 5a-b).

In order to understand the mechanism for the improved structural stability of the 2D $Zr_3C_2T_z$, the binding energy describing structure stability were studied. The bare 2D Ti_3C_2 and Zr_3C_2 MXenes, together with the bulk TiC and ZrC crystals were investigated. The binding energy is defined as follows:

$$E_{binding} = (\sum_i n_i E_{atom} - E_{system}) / \sum_i n_i \qquad (4),$$

where n_i is the atom number for each type atom. E_{atom} is the energy of an isolated atom, and E_{system} is the total energy of the system investigated. The binding energies of our four investigated materials are given in Table S1. Our results show that the binding energy of the bulk TiC is determined to be 8.741 eV, which is larger than that 8.080 eV of Ti_3C_2 MXene. Thus, the Ti_3C_2 MXene is inclined to transform into the more stable TiC configuration under high temperature as the experimental results.[15] However, 2D Zr_3C_2 presents a slightly higher binding energy than that of bulk ZrC, and thus the 2D $Zr_3C_2T_z$ MXene can easier retain its 2D nature at elevated temperatures. The above calculated binding energy well explains the difference in structure stabilities between the $Ti_3C_2T_z$ and $Zr_3C_2T_z$ MXenes. Due to the higher stability, the 2D $Zr_3C_2T_z$ may be useful for potential applications under high temperature conditions.

Table 1 The structural parameters and elastic constants of the 2D $Zr_3C_2T_2$ (T=O,F, and OH).

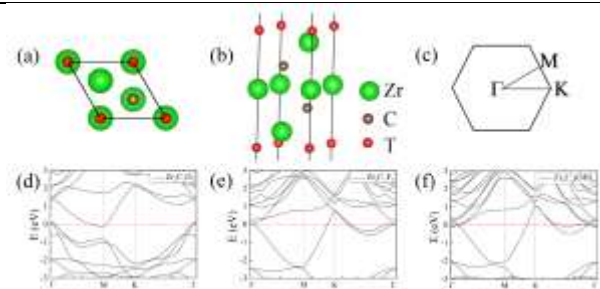| System	a (Å)	d (Å)	c_{11} (GPa)	c_{12} (GPa)
Ti_3C_2	3.097	7.237	335.5	66.29
Zr_3C_2	3.336	7.990	295.2	60.93
$Zr_3C_2O_2$	3.314	9.475	392.9	117.7
$Zr_3C_2F_2$	3.332	10.19	293.0	75.68
$Zr_3C_2(OH)_2$	3.330	11.31	270.4	64.69

Figure 7 (a) and (b) are the top-view and side-view of the 2D $Zr_3C_2T_2$ (T=O, F, OH). (c) is the Brillouin zone of the 2D hexagonal lattice. (d), (e) and (f) are the electronic energy bands of the $Zr_3C_2O_2$, $Zr_3C_2F_2$ and $Zr_3C_2(OH)_2$, respectively.

Since MXenes are normally functionalized by the oxygen, fluorine and hydroxyl groups[20, 44] we further investigated the basic structural, mechanical and electronic properties of the monolayer $Zr_3C_2T_2$ (T=O,F,OH). Considering four different structural models followed by Xie's work,[45] the stable atomic configurations of the 2D $Zr_3C_2T_2$ were all determined.

The top-view and side-view of the 2D $Zr_3C_2T_2$ are given in Figure 7a and 7b, respectively. The functional groups T are on the top-sites of the middle zirconium atoms. The space group of our unit cell is P $\bar{3}$ m1 (164), and the corresponding Brillouin zone (BZ) of the 2D hexagonal lattice is given in Figure 7c. The relaxed lattice parameters of the three 2D carbides investigated are given in the second column of Table 1. Evidently, the oxygen functionalized $Zr_3C_2O_2$ presents a smaller lattice parameter compared to those of $Zr_3C_2F_2$ and $Zr_3C_2(OH)_2$. This behavior is due to the stronger interaction between the oxygen groups and the surface zirconium atoms, and which has been well studied for the M_2CT_2 MXenes in our previous work.[44] The mechanical strengths of the $Zr_3C_2T_2$ and the bare M_3C_2 (M=Ti, Zr) MXenes meantioned were also determined, which were calculated from Equation (5):

$$c_{ij} = c_{ij,cell}(c/d) \tag{5}$$

where $c_{ij,cell}$ is the elastic constants estimated from the MXene unit cell, c is the lattice parameter perpendicular to MXene surface, and it is equal to 30 Å in our simulation. d is the layer thickness, which is chosen as the distance between the top-surfaces of two neighboring monomers in the multilayer MXenes, similar to the work of Fei and Yang for phosphorene.[46] All the layer thicknesses (d), the calculated elastic constants c_{11} and c_{12} are given in Table 1. The layer thicknesses presented here are monolayer thicknesses without considering intercalated species, and are thus smaller than the experimental results. The mechanical strength c_{11} for $Zr_3C_2O_2$ is determined as high as 392.9 GPa. This manifests that the $Zr_3C_2O_2$ can be a good choice used in composite structural materials. The electronic energy bands of the 2D $Zr_3C_2T_2$ (T=O, F, OH) are provided in Figure 7e-f are the electronic energy bands of the 2D $Zr_3C_2O_2$, $Zr_3C_2F_2$ and $Zr_3C_2(OH)_2$, respectively. All of the three 2D carbides are metallic with electronic energy branches crossing their Fermi levels.

In summary, we synthesized the 2D $Zr_3C_2T_x$ MXene for the first time from parent ternary layered $Zr_3Al_3C_5$, which provides a new approach for the synthesis of Zr- and potentially Hf- containing MXenes. Based on DFT calculations, the structural, electronic and elastic properties of our obtained $Zr_3C_2T_z$ MXenes have been well determined. All of the three functionalized $Zr_3C_2T_2$ (T=O, F, OH) MXenes exhibit metallic behavior, and $Zr_3C_2O_2$ presents the strongest mechanical strength withthe c_{11} value of 392.9 GPa. Compared to $Ti_3C_2T_z$ MXene, $Zr_3C_2T_z$ was demonstrated to have better structural stability in vacuum or argon atmosphere. It is reasonable to assume that this newly developed 2D $Zr_3C_2T_z$ MXenes will have promising potential applications range from electrode materials in electrical energy storage, reinforcement fillers for polymers, to sensors and catalysts, especially when served in relatively high temperature environment.

Acknowledgements

[1] K. S. Novoselov, A. K. Geim, S. V. Morozov, D. Jiang, Y. Zhang, S. V. Dubonos, I. V. Grigorieva, A. A. Firsov, *Science* **2004**, *306*, 666-669.

[2] H. Zhang, *ACS nano* **2015**, *9*, 9451-9469.

[3] M. Xu, T. Liang, M. Shi, H. Chen, *Chem. Rev.* **2013**, *113*, 3766-3798.

[4] M. Naguib, Y. Gogotsi, *Acc. Chem. Res.* **2015**, *48*, 128-135.

[5] V. Singh, D. Joung, L. Zhai, S. Das, S. I. Khondaker, S. Seal, *Prog. Mater Sci.* **2011**, *56*, 1178-1271.

[6] A. Gupta, T. Sakthivel, S. Seal, *Prog. Mater Sci.* **2015**, *73*, 44-126.

[7] J. N. Coleman, M. Lotya, A. O'Neill, S. D. Bergin, P. J. King, U. Khan, K. Young, A. Gaucher, S. De, R. J.Smith, I. V. Shvets, S. K. Arora, G. Stanton, H.-Y. Kim, K. Lee, G. T. Kim, G. S. Duesberg, T. Hallam, J. J. Boland, J. J. Wang, J. F. Donegan, J. C. Grunlan, G. Moriarty, A. Shmeliov, R. J. Nicholls, J. M. Perkins, E. M. Grieveson, K. Theuwissen, D. W. McComb, P. D. Nellist, V. Nicolosi, *Science* **2011**, *331*, 568-571.

[8] R. C. Andrew, R. E. Mapasha, A. M. Ukpong, N. Chetty, *Physical Review B* **2012**, *85*, 125428.

[9] C. Lee, X. Wei, J. W. Kysar, J. Hone, *Science* **2008**, *321*, 385-388.

[10] A. H. Castro Neto, F. Guinea, N. M. R. Peres, K. S. Novoselov, A. K. Geim, *Reviews of Modern Physics* **2009**, *81*, 109-162.

[11] A. A. Balandin, S. Ghosh, W. Bao, I. Calizo, D. Teweldebrhan, F. Miao, C. N. Lau, *Nano Lett.* **2008**, *8*, 902-907.

[12] Y. Zhu, S. Murali, W. Cai, X. Li, J. W. Suk, J. R. Potts, R. S. Ruoff, *Adv. Mater.* **2010**, *22*, 3906-3924.

[13] S. Z. Butler, S. M. Hollen, L. Cao, Y. Cui, J. A. Gupta, H. R. Gutiérrez, T. F. Heinz, S. S. Hong, J. Huang, A. F. Ismach, E. Johnston-Halperin, M. Kuno, V.V. Plashnitsa, R. D. Robinson, R. S. Ruoff, S. Salahuddin, J. Shan, L. Shi, M. G. Spencer, M. Terrones, W. Windl, J. E. Goldberger, *ACS nano* **2013**, *7*, 2898-2926.

[14] M. Naguib, V. N. Mochalin, M. W. Barsoum, Y. Gogotsi, *Adv. Mater.* **2014**, *26*, 982-982.

[15] M. W. Barsoum, *Prog. Solid State Chem.* **2000**, *28*, 201-281.

[16] P. Eklund, M. Beckers, U. Jansson, H. Högberg, L. Hultman, *Thin Solid Films* **2010**, *518*, 1851-1878.

[17] M. Naguib, O. Mashtalir, J. Carle, V. Presser, J. Lu, L. Hultman, Y. Gogotsi, M. W. Barsoum, *ACS nano* **2012**,

6, 1322-1331.

[18] J. Halim, M. R. Lukatskaya, K. M. Cook, J. Lu, C. R. Smith, L.-Å. Näslund, S. J. May, L. Hultman, Y. Gogotsi, P. Eklund, M. W. Barsoum, *Chem. Mater.* **2014**, *26*, 2374-2381.

[19] M. Naguib, M. Kurtoglu, V. Presser, J. Lu, J. Niu, M. Heon, L. Hultman, Y. Gogotsi, M. W. Barsoum, *Adv.Mater.* **2011**, *23*, 4248-4253.

[20] M. Khazaei, M. Arai, T. Sasaki, C.-Y. Chung, N. S. Venkataramanan, M. Estili, Y. Sakka, Y. Kawazoe, *Adv. Funct. Mater.* **2013**, *23*, 2185-2192.

[21] H. Fashandi, V. Ivády, P. Eklund, A. L. Spetz, M. I. Katsnelson, I. A. Abrikosov, *Physical Review B* **2015**, *92*, 155142.

[22] M. R. Lukatskaya, O. Mashtalir, C. E. Ren, Y. Dall'Agnese, P. Rozier, P. L. Taberna, M. Naguib, P. Simon, M. W. Barsoum, Y. Gogotsi, *Science* **2013**, *341*, 1502-1505.

[23] X. Liang, A. Garsuch, L. F. Nazar, *Angew. Chem. Int. Ed.* **2015**, *54*, 3907-3911.

[24] M. Naguib, J. Come, B. Dyatkin, V. Presser, P.-L. Taberna, P. Simon, M. W. Barsoum, Y. Gogotsi, *Electrochem. Commun.* **2012**, *16*, 61-64.

[25] X. Wang, S. Kajiyama, H. Iinuma, E. Hosono, S. Oro, I. Moriguchi, M. Okubo, A. Yamada, *Nat Commun* **2015**,*6*.

[26] M. Naguib, J. Halim, J. Lu, K. M. Cook, L. Hultman, Y. Gogotsi, M. W. Barsoum, *J. Am. Chem. Soc.* **2013**, *135*, 15966-15969.

[27] M. Ghidiu, M. R. Lukatskaya, M.-Q. Zhao, Y. Gogotsi, M. W. Barsoum, *Nature* **2014**, *516*, 78-81.

[28] B. Anasori, Y. Xie, M. Beidaghi, J. Lu, B. C. Hosler, L. Hultman, P. R. C. Kent, Y. Gogotsi, M. W. Barsoum, *ACS nano* **2015**, *9*, 9507-9516.

[29] R. Meshkian, L.-Å. Näslund, J. Halim, J. Lu, M. W. Barsoum, J. Rosen, *Scripta Mater.* **2015**, *108*, 147-150.

[30] C. Hu, C. C. Lai, Q. Tao, J. Lu, J. Halim, L. Sun, J. Zhang, J. Yang, B. Anasori, J. Wang, Y. Sakka, L. Hultman, P. Eklund, J. Rosen, M. W. Barsoum, *Chem. Commun.* **2015**, *51*, 6560-6563.

[31] C. C. Lai, R. Meshkian, M. Dahlqvist, J. Lu, L. Å. Näslund, O. Rivin, E. N. Caspi, O. Ozeri, L. Hultman, P. Eklund, M. W. Barsoum, J. Rosen, *Acta Mater.* **2015**, *99*, 157-164.

[32] C. Xu, L. Wang, Z. Liu, L. Chen, J. Guo, N. Kang, X.-L. Ma, H.-M. Cheng, W. Ren, *Nat Mater* **2015**, *14*, 1135-1141.

[33] Y.-C. Zhou, L.-F. He, Z.-J. Lin, J.-Y. Wang, *J. Eur. Ceram. Soc.* **2013**, *33*, 2831-2865.

[34] J. Zhou, F. Qiu, L. Shen, F. Li, J. Xue, M. W. Barsoum, Q. Huang, *J. Am. Ceram. Soc.* **2014**, *97*, 1296-1302.

[35] O. Mashtalir, M. Naguib, V. N. Mochalin, Y. Dall'Agnese, M. Heon, M. W. Barsoum, Y. Gogotsi, *Nat Commun* **2013**, *4*, 1716.

[36] Q. Tang, Z. Zhou, *Prog. Mater Sci.* **2013**, *58*, 1244-1315.

[37] C. Morant, J. M. Sanz, L. Galán, L. Soriano, F. Rueda, *Surf. Sci.* **1989**, *218*, 331-345.

[38] A. P. Rizzato, C. V. Santilli, S. H. Pulcinelli, Y. Messaddeq, P. Hammer, *J. Sol-Gel Sci. Technol.* **2004**, *32*,155-160.

[39] M.-P. Crosnier-Lopez, F. Le Berre, J.-L. Fourquet, *J. Mater. Chem.* **2001**, *11*, 1146-1151.

[40] J. Li, Y. Du, C. Huo, S. Wang, C. Cui, *Ceram. Int.* **2015**, *41*, 2631-2635.

[41] Z. Li, L. Wang, D. Sun, Y. Zhang, B. Liu, Q. Hu, A. Zhou, *Materials Science and Engineering: B* **2015**, *191*, 33-40.

[42] T. El-Raghy, M. W. Barsoum, M. Sika, *Materials Science and Engineering: A* **2001**, *298*, 174-178.

[43] M. W. Barsoum, T. El‑Raghy, L. Farber, M. Amer, R. Christini, A. Adams, *J. Electrochem. Soc.* **1999**, *146*, 3919-3923.

[44] X. H. Zha, K. Luo, Q. Li, Q. Huang, J. He, X. Wen, S. Du, *EPL (Europhysics Letters)* **2015**, *111*, 26007.

[45] Y. Xie, P. R. C. Kent, *Physical Review B* **2013**, *87*, 235441.

[46] R. Fei, L. Yang, *Nano Lett.* **2014**, *14*, 2884.

Layout 2:

COMMUNICATION
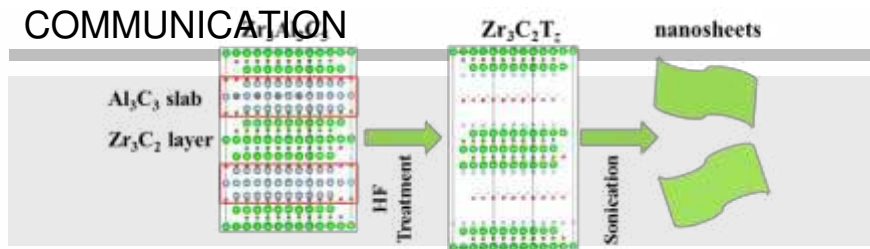
Jie Zhou, Xian H. Zha, Fan Y. Chen, Qun Ye, Per Eklund, Shiyu Du,* and Qing Huang*_____1-6

A New Two-Dimensional Zirconium Carbide MXene by selective etching of Al₃C₃ from nanolaminated Zr₃Al₃C₅

$Zr_3C_2T_z$ nanosheets: A new two-dimensional (2D) zirconium-containing carbide, $Zr_3C_2T_z$ MXene is obtained through selective etching of Al_3C_3 units from layered ternary $Zr_3Al_3C_5$ beyond MAX phases (see figure) at room temperature. The structural, mechanical and electronic properties of the synthesized 2D carbide are investigated combined with first-principles density functional calculations. Noteworthily, the obtained 2D $Zr_3C_2T_z$ exhibits excellent thermal stability, which stably exists even at 1200℃ in vacuum.

Supporting Information

A New Two-Dimensional Zirconium Carbide MXene by Selective Etching of Al$_3$C$_3$From Nanolaminated Zr$_3$Al$_3$C$_5$

Jie Zhou[1], Xian H. Zha[1], Fan Y. Chen[1], Qun Ye[1], Per Eklund[2], Shiyu Du[1,*]and Qing Huang[1,*]

[1]Engineering Laboratory of Specialty Fibers and Nuclear Energy Materials (FiNE), Ningbo Institute of Materials Engineering and Technology, Chinese Academy of Sciences, Ningbo,Zhejiang 315201, China

[2]Thin Film Physics Division, Linköping University, IFM, 581 83 Linköping, Sweden

S1. Experimental Section

Preparation of Zr$_3$Al$_3$C$_5$ powders: The Zr$_3$Al$_3$C$_5$ powders were prepared by pulsed electric current sintering (PECS) of Zr/Al/graphite powder mixtures according to our previous study.[1] In detail, the as-received commercially elemental powders were weighed with a molar ratio of Zr:Al:C, 3:3.2:4.8, respectively, and blended in a polyethylene jar for 12 h in a planetary ball mill at a rate of 200 rpm with absolute ethanol and agate balls as grinding media. The powders were then dried at 50°C for 24 h. The resulting homogenous mixture was poured into a graphite die (40 mm in diameter) and cold pressed to load corresponding to a pressure of 5 MPa. Subsequently the green body, together with the die, was heated in a PECS apparatus (HP D25/1, FCT System GmbH, Germany) to1800°C for 20 min with holding pressure of 30Mpa in an Ar atmosphere.After cooling to room temperature, bulk samples were pulverized and sieved through a 300-mesh screen.

Preparation of Ti$_3$AlC$_2$ powders: The Ti$_3$AlC$_2$ powders were prepared by pulsed electric current sintering (PECS) of Ti/Al/graphite powder mixtures according to the reference.[2] In detail, the as-received commercially elemental powders were weighed with a molar ratio of Ti:Al:C=3:1.2:0.9, respectively. The resulting powders were ball-milled for 16 h in a planetary ball mill at a rate of 250 rpm with absolute ethanol and agate balls as grinding media. The powders were then dried at 50°C for 24 h. The resulting powder mixture was poured into a graphite die (40 mm in diameter) and cold pressed to load corresponding to a pressure of 5 MPa. Subsequently the green body, together with the die, was heated in a PECS apparatus (HP D25/1, FCT System GmbH, Germany) to 1280°C for 20 min with holding pressure of 30Mpa in an Ar atmosphere. After cooling to room temperature, bulk samples were pulverized and sieved through a 300-mesh screen.

Preparation of two dimentional(2D) Zr$_3$C$_2$T$_z$ nanosheets: Roughly 1g of the as-prepared 300-mesh Zr$_3$Al$_3$C$_5$ powders was immersed in 10 ml of a 50 wt.% HF solution at room temperature for 72 h. Then the resulting suspension was cleaned by deionized water and alcohol for several times and filtered with microfiltration

membrane (polyvinylidene fluoride，PVDF, 0.45μm, Shanghai Xinya) to separate the powders. The obtained powders were dried at room temperature for 48 h.

Preparation of two dimentional(2D) Ti₃C₂Tz nanosheets: The $Ti_3C_2T_x$ was synthesized by immersing 1 g of Ti_3AlC_2 powders in 10 ml of 50% concentrated HF solution for 40 h at room temperature[3] and filtered with microfiltration membrane (polyvinylidene fluoride，PVDF, 0.45μm, Shanghai Xinya) to separate the powders. The obtained powders were then dried at room temperature for 48 h.

High temperature vacuum annealing treatment: Roughly 0.1g of the as-prepared 2D $Ti_3C_2T_x$ and $Zr_3C_2T_x$ nanosheets were heated from room temperature to 1273K under vacuum of 2E-2Pa for 2h in an tube furnace.

Preparation of exfoliated Zr₃C₂Tz flakes for TEM and AFM analysis: The as-etched powders were sonicated in ethanol for about 6h, and then centrifuged to obtain the supernatant. Before AFM and TEM measurement, the supernatant was sonicated for another 10 minutes, then droplets from the supernatant were left to dry on a silicon wafer (p(100)) for AFM study, and on a lacey-carbon coated copper grid (200 mesh) for TEM study, respectively.

Characterization: The phase composition of the as-prepared samples was analyzed by X-ray diffractometer, XRD, (D8 Advance, Bruker AXS, Germany) with Cu K_α radiation. XRD data were collected at a step size of 0.02°/2θ with a collection time of 1s per step. The powders were cold pressing to 10MPa for XRD. The microstructure and chemical composition were observed by Field Emission Scanning Electron Microscope, FESEM (QUANTA 250 FEG, FEI, USA) coupled with an energy dispersive spectrometer (EDS). The chemical state of the materials before and after exfoliation was analyzed by X-ray photoelectron spectroscopy, XPS (AXISUltra DLD, Kratos, Japan). Transmission electron microscopy (TEM) and high-resolution TEM images were carried out on a Tecnai F20 (FEI, USA) electron microscope at an acceleration voltage of 200 kV. Atomic force microscopy (AFM) analysis was performed by means of Dimension 3100V system (Veeco, USA) under tapping mode. Thermal stability of the obtained MXenes was investigated by simultaneous thermal

analyzer (STA, 449 F3, Netzsch, Germany)with α-Al_2O_3 crucible under argon flow at a heating rate of 10 ◦C/min from room temperature to 1200◦C.

Calculation details: All our calculations were performed using the plane-wave VASP code.[4-5] The generalized gradient approximation (GGA)[6] with the Perdew-Burke-Ernzerhof (PBE) exchange and correlation functional was adopted. The projector augmented wave (PAW)[7] potentials with a plane-wave energy cutoff of 500 eV was employed to describe the electron-core interaction. The structure optimization was based on the conjugate gradient algorithm. All the structures were relaxed until the forces on each atom were smaller than 0.01 eV/atom, and the criterion of energy convergence was 1.0×10^{-5} eV/cell. A $12 \times 12 \times 1$ k-points mesh was adopted in the Brillouin zone (BZ) of the hexagonal unit cell. To eliminate the layer interaction, a 30 Å lattice parameter perpendicular to the layer surface was adopted for monolayer MXenes. For plotting electronic energy bands, 60 k-points sampled in the BZ were employed. To accurately describe the interlayer interaction of the multilayers, a damped van der Waals (vdW) correction (DFT-D2)[8] was adopted in determining the layer thickness. All the structures are visualized using the VESTA code.[9]

In Model A and Model B, their lattice parameters in the xy planeare chosen as the same as that in the $Zr_3Al_3C_5$ structure. Enough vacuum space (10 Å) is adopted between the separated Zr-C and Al-C layers. During structural optimization, the lattices of the two models are fixed, which is different from those MXenes' relaxation with both the lattice parameters and atomic configurations optimized.

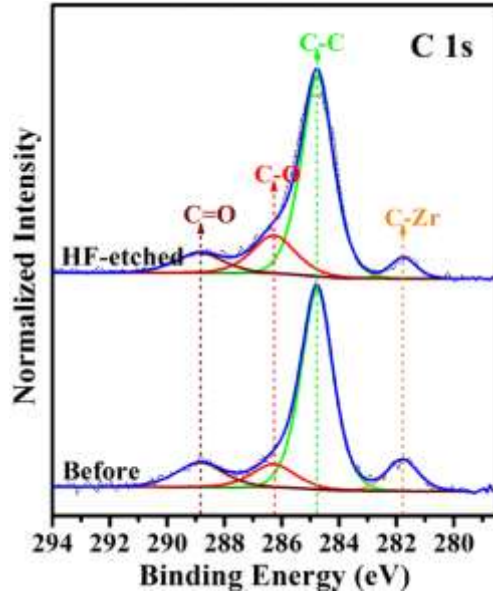## S2. Additional information on $Zr_3C_2T_z$ nanosheets

Figure S1 High-resolution C 1s XPS spectra of samples before and after HF treatment.

The spectra of the $Zr_3Al_3C_5$ and $Zr_3C_2T_z$ samples were taken without Ar sputtering. All binding energies were referenced to that of free carbon at 284.6 eV. A high-resolution spectrum of the $Zr_3C_2T_z$ layers in the C 1s region (Figure S1) could be fit with the four components: a low-binding energy peak (5.6% of C 1s photoemission, 281.8 eV) that corresponds to C in Zr_3C_2.[10-11] With another two corresponding to adventitious contamination (17.28% of C 1s photoemission, 286.1 eV, and 67.1% of C 1s photoemission, 284.8 eV), a high-binding energy peak might be attributed to adsorbed methanol (9.9% of C 1s photoemission, 288.8 eV).[12] The large amount of contamination and low intensity of the Zr_3C_2 signal might be related to the lack of Ar etching. As illustrated in Figure S1, for the as-prepared $Zr_3Al_3C_5$ powders, A high-resolution spectrum in the C 1s region could also be fit with the above four components, and the content corresponding to C in $Zr_3Al_3C_5$ is about 10.43%.
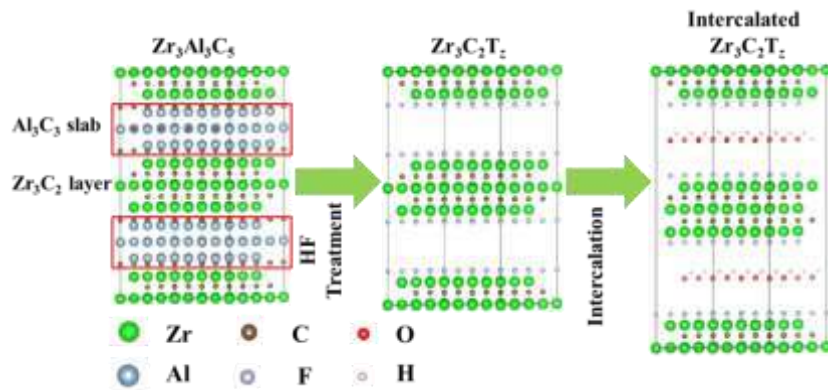

Figure S2 Schematic illustration of the exfoliation process for $Zr_3Al_3C_5$ under hydrofluoric acid treatment. a) crystal structure of $Zr_3Al_3C_5$. b) Al-C units replaced by OH and F after reaction with HF. c) intercalation of water molecules and reaction products.
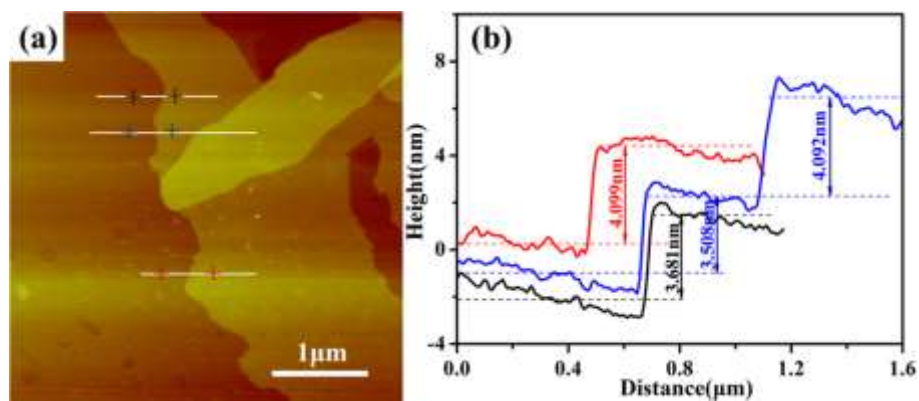
Figure S3 a) AFM topography image of $Zr_3C_2T_z$ nanosheets, and b) the corresponding height measurement.

Table S1 The total and binding energies of Ti_3C_2 and Zr_3C_2 MXenes, and bulk TiC and ZrC.

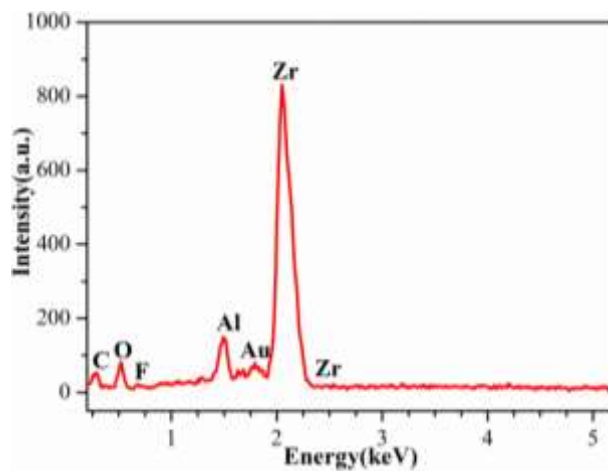| System	Atom number	Total energy (eV)	Binding energy (eV)
Ti_3C_2	5	-43.52	8.080
TiC	8	-74.10	8.741
Zr_3C_2	5	-46.06	8.483
ZrC	8	-72.59	8.468

Figure S4 The EDS analysis results of the HF-etched powders, and the corresponding molar ratio of Zr:C:O:F:Al approximate 3:1.91:1.16:0.11:0.44.
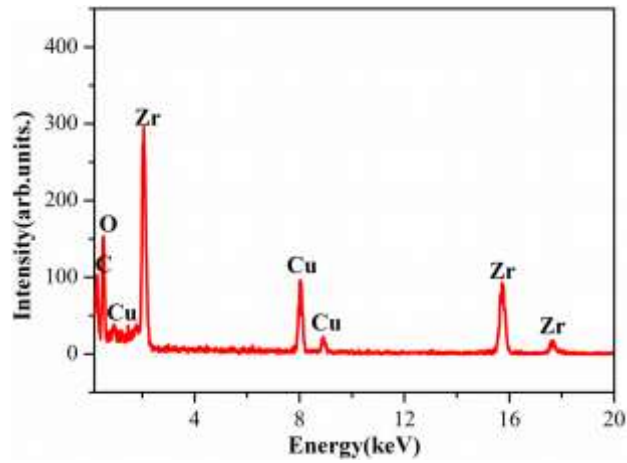
Figure S5 The EDS analysis results of the $Zr_3Al_3C_5$ after HF treatment observed in TEM.
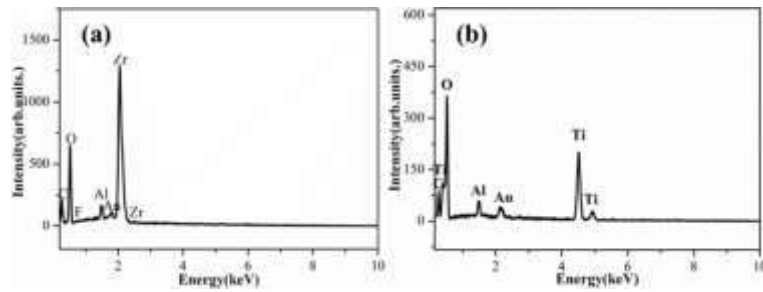

Figure S6 EDS analysis results of the $Zr_3C_2T_z$ (a) and $Ti_3C_2T_z$ (b) powders after high temperature vacuum annealing.

References:

[1] J. Zhou, F. Qiu, L. Shen, F. Li, J. Xue, M. W. Barsoum, Q. Huang, *J. Am. Ceram. Soc.* **2014**, *97*,1296-1302.

[2] C. Yang, S. Jin, B. Liang, G. Liu, L. Duan, S. Jia, *J. Alloys Compd.* **2009**, *472*, 79-83.

[3] M. Naguib, M. Kurtoglu, V. Presser, J. Lu, J. Niu, M. Heon, L. Hultman, Y. Gogotsi, M. W. Barsoum, *Adv. Mater.* **2011**, *23*, 4248-4253.

[4] G. Kresse, J. Furthmüller, *Physical Review B* **1996**, *54*, 11169-11186.

[5] G. Kresse, J. Furthmüller, *Computational Materials Science* **1996**, *6*, 15-50.

[6] J. P. Perdew, K. Burke, M. Ernzerhof, *Phys. Rev. Lett.* **1996**, *77*, 3865-3868.

[7] P. E. Blöchl, *Physical Review B* **1994**, *50*, 17953-17979.

[8] S. Grimme, *J. Comput. Chem.* **2006**, *27*, 1787-1799.

[9] K. Momma, F. Izumi, *J. Appl. Crystallogr.* **2011**, *44*, 1272-1276.

[10] C. Morant, J. M. Sanz, L. Galán, L. Soriano, F. Rueda, *Surf. Sci.* **1989**, *218*, 331-345.

[11] A. Escudeiro, N. M. Figueiredo, T. Polcar, A. Cavaleiro, *Appl. Surf. Sci.* **2015**, *325*, 64-72.

[12] M. Naguib, J. Halim, J. Lu, K. M. Cook, L. Hultman, Y. Gogotsi, M. W. Barsoum, *J. Am. Chem. Soc.* **2013**, *135*, 15966-15969.